JOURNAL OF SPACECRAFT AND ROCKETS
Vol. 45, No. 2, March–April 2008

Autonomous Optical Navigation at Jupiter: A Linear Covariance Analysis

Nathan B. Stastny* and David K. Geller†
Utah State University, Logan, Utah 84322

DOI: 10.2514/1.28451

On 24 October 1998 NASA launched Deep Space 1, an experimental interplanetary spacecraft used to validate future technologies including an autonomous optical navigation system. Before Deep Space 1, interplanetary navigation was performed primarily through Earth-based measurements to provide accurate position and velocity estimates of the spacecraft. Improvements in imaging and computing technologies, enabling onboard processing and orbit determination, have lead to expanded interest in autonomous spacecraft. Development of autonomous optical navigation systems for interplanetary spacecraft requires extensive modeling and analysis to ensure success. This paper, using a linear covariance analysis, evaluates the efficacy of using optical angles-only measurements of the moons of Jupiter to determine a spacecraft's position and velocity during a Jupiter approach. The analysis also evaluates the dominant error sources in the orbit determination calculations for preflight performance evaluations.

Nomenclature

$[\mathbf{A}\times]$	=	cross product matrix defined by $[\mathbf{A}\times]\mathbf{B} = \mathbf{A} \times \mathbf{B}$
B	=	true body
B_N	=	nominal body
C	=	true camera
C_N	=	nominal camera
d_0	=	one astronomical unit
d_{MS}	=	distance from the sun to the Jovian moon
d_{MSC}	=	distance from the spacecraft to the Jovian moon
H	=	absolute magnitude
I	=	Jupiter centered inertial
m	=	apparent visual magnitude
$\mathbf{R}_J$	=	Jupiter position vector relative to the sun
$\mathbf{R}_m$	=	Jovian moon position vector relative to Jupiter
$\mathbf{R}_{\mathrm{sc}}$	=	spacecraft position vector relative to Jupiter
T_a^b	=	direction cosine matrix from the a frame to the b frame
χ	=	moon phase angle relative to the spacecraft
$\hat{\mathbf{x}}$	=	estimated state vector
$\bar{\mathbf{x}}$	=	nominal state vector

Subscripts

k	=	discrete time step
rel	=	Jovian moon position relative to the spacecraft
sc	=	spacecraft

Superscripts

$+$	=	postupdate
$-$	=	preupdate

Presented as Paper 6680 at the AIAA/AAS Astrodynamics Specialist Conference and Exhibit, Keystone, Colorado, 21–24 August 2006; received 20 October 2006; revision received 4 October 2007; accepted for publication 4 October 2007.

*Graduate Student, Mechanical and Aerospace Engineering Department. Member AIAA.

†Assistant Professor, Mechanical and Aerospace Engineering Department. Senior Member AIAA.

I. Introduction

OPTICAL navigation, the foundation for most terrestrial navigation, has remained a mainstay of exploration even into the Space Age. Aspects of optical navigation were employed on the Apollo missions [1]. The first interplanetary spacecrafts to depend on optical navigation for mission success were Voyager I and Voyager II [2]. The first Voyager encounter was in March 1979 when Voyager I navigated past Jupiter on its grand tour. Optical navigation methods were also used by the Voyager spacecraft for encounters with Saturn, Uranus, and Neptune, as well as 48 of their moons [3–6]. Although optical navigation techniques have been used extensively on interplanetary spacecraft to improve state estimates, the spacecraft generally depended on the Deep Space Network (DSN) and ground processing of data for state estimation. The first spacecraft to attempt autonomous optical navigation was Deep Space 1 (DS1) [7,8]. As a technology validation mission, the autonomous optical navigation (AutoNav) system was given some oversight through the DSN and ground processing to evaluate the system's performance. The DS1 mission successfully validated the AutoNav system while exploring the asteroid Braille in July 1999 and the comet Borrelly in September 2001. NASA's Mars Reconnaissance Orbiter, launched in August 2005, is equipped with an experimental optical navigation camera for imaging Mars's two moons, Deimos and Phobos, and providing improvements to the spacecraft's Mars-relative orbit determination (OD). It is anticipated that future interplanetary spacecraft will require increased autonomy, including autonomous navigation techniques. Autonomous navigation reduces mission oversight requirements and improves time critical operations such as flybys or atmospheric entry.

This study is a preliminary performance analysis of an interplanetary spacecraft at Jupiter that employs new autonomous optical navigation techniques. It is proposed that the spacecraft's autonomous optical navigation system use line-of-sight measurements to the moons of Jupiter for orbit determination. Use of the moons as "optical beacons" for a Jupiter approach can be thought of as a pseudo-GPS (global positioning system). The objective of the research is to determine the efficacy of such a system and the dominant design parameters for possible future missions. The research also evaluates the sensitivity of the OD to predetermined problem parameters and attempts to determine the primary sources of navigation error. For additional outer planet navigation studies, the reader is referred to the works of Ondrasik and Ransford [9] and Russell and Ellis [10].

Analysis of the proposed AutoNav system is performed through a linear covariance (LinCov) analysis [11] that can be used to determine changes in a navigation system's performance by adjusting the inputs and parameters of the estimation filter. Linear

covariance techniques are not new and are often used in OD studies to determine navigation errors and parameter sensitivities [12–15].

The research analyzes the spacecraft during a hyperbolic approach to Jupiter, similar to that proposed for NASA's Juno New Frontiers mission [16], and a Jupiter orbit insertion maneuver. The work also includes the use of a high-fidelity model of the Jovian system with a large number of its moons.

II. Methods

To evaluate the optical navigation technique, it is necessary to develop a reasonably accurate truth model and simulation. The truth model includes two parts: 1) a high-accuracy ephemeris model of Jupiter and its moons, and 2) a nominal approach trajectory starting at Jupiter's sphere of influence (SOI). It is proposed for this analysis that the onboard AutoNav system employ a continuous–discrete extended Kalman filter [11]. Analysis of the AutoNav system's performance is evaluated using a LinCov analysis.

A. Jovian Moon Ephemerides

The ephemeris model for the Jovian system is based on the SPICE information system provided by NASA's Navigation and Ancillary Information Facility (NAIF). SPICE is an analysis and planning tool developed by NAIF to aid the scientific community in evaluating mission science and archiving scientific data. Among the archived data are planetary ephemerides derived from high-fidelity models. Given the available SPICE data, 38 Jovian moons [JI (Io) through JXXXVIII (Pasithee) by Roman numeral designation] were considered as possible navigation beacons. Jupiter is currently known to have 63 moons.

B. Nominal Spacecraft Trajectory

The nominal spacecraft trajectory is a hyperbolic approach beginning at Jupiter's SOI and running through perijove. Perijove for the approach occurs at a radius of approximately 1.06 Jupiter radii [16]. The trajectory, varying from the proposed Juno transit, is based on a 2010 launch and a total transit of 665 days. The Jupiter relative approach eccentricity is 1.035. The spacecraft's velocity at SOI is 6.653 km/s.

The gravitational model of Jupiter used to develop the trajectory and simulation is a point mass plus J_2 model. The model does not account for higher order perturbation terms or third body perturbations. It is important to note that a higher fidelity gravity model would be required in an actual onboard filter to accurately define the spacecraft's dynamics. Use of the simplified model, however, will not affect the navigation analysis results obtained in this study, because random accelerations, modeled as white noise, are added to account for the difference between the onboard gravity model and the true gravity.

C. Kalman Filter Conceptual Design

Kalman filters are commonly used in space navigation applications and are well suited for AutoNav systems. The evaluated system's state vector includes the spacecraft's position and velocity as well as sensor misalignments, $\boldsymbol{\epsilon}$, and a nonconstant attitude knowledge error, $\delta\boldsymbol{\theta}$.

$$\mathbf{x} = [\mathbf{R}^I_{\text{sc}},\ \ \mathbf{V}^I_{\text{sc}},\ \ \boldsymbol{\epsilon},\ \ \delta\boldsymbol{\theta}]^T \tag{1}$$

The nonlinear system dynamics and measurement models for the state vector are

$$\dot{\mathbf{x}}(t) = \mathbf{f}[\mathbf{x}(t), t] + \mathbf{w}(t) \tag{2}$$

and

$$\mathbf{z}_k = \mathbf{h}_k[\mathbf{x}(t_k)] + \mathbf{v}_k \tag{3}$$

where the dynamics for the state vector are given by

$$\dot{\mathbf{R}}^{\ I}_{\text{sc}} = \mathbf{V}^I_{\text{sc}} \tag{4}$$

$$\dot{\mathbf{V}}^{\ I}_{\text{sc}} = \mathbf{a}^I_{\text{grav}} + \mathbf{a}_o \tag{5}$$

$$\dot{\boldsymbol{\epsilon}} = 0 \tag{6}$$

$$\delta\dot{\boldsymbol{\theta}} = -\frac{\delta\boldsymbol{\theta}}{\tau_{\delta\theta}} + \mathbf{w}_{\delta\theta} \tag{7}$$

The gravitational acceleration of the vehicle, $\mathbf{a}^I_{\text{grav}}$, represents the onboard gravity model, or the point mass plus J_2 used for the analysis. Additional random accelerations $\mathbf{a}_o$ are used to represent modeling errors. The covariances of these disturbances are $E[\mathbf{a}_o(t)\mathbf{a}_o^T(t')] = Q_a\delta(t-t')$, where Q_a represents the strength of the corresponding white noise. The misalignment error is constant. The attitude knowledge error is modeled as a first-order Markov process driven by white noise $\mathbf{w}_{\delta\theta}$, with a covariance $E[\mathbf{w}_{\delta\theta}(t)\mathbf{w}^T_{\delta\theta}(t')] = Q_{\delta\theta}\delta(t-t')$. The time constant $\tau_{\delta\theta}$ is set to 1 h, which corresponds to the estimated time between attitude updates from a star camera.

The camera line-of-sight measurements $\mathbf{z}_k$ are given by [17]

$$\mathbf{z}_k = \begin{bmatrix} R_x/R_z \\ R_y/R_z \end{bmatrix} + \boldsymbol{\nu}_k \tag{8}$$

where the relative position of the imaged moon in the camera frame, $\mathbf{R}^C_{\text{rel}} = [R_x, R_y, R_z]^T$, is given by

$$\mathbf{R}^{\ C}_{\text{rel}} = \mathbf{T}^C_{C_N}\mathbf{T}^{C_N}_B\mathbf{T}^B_{B_N}\mathbf{T}^{B_N}_I\left(\mathbf{R}^I_{\text{moon}} - \mathbf{R}^I_{\text{sc}}\right) \tag{9}$$

and the covariance of the measurement noise is $E[\boldsymbol{\nu}_k(t_k)\boldsymbol{\nu}^T_k(t'_k)] = R_{\nu_k}\delta(t_k - t'_k)$. Using a small angle approximation for the camera misalignment and attitude knowledge errors, the relative position can be rewritten as

$$\mathbf{R}^{\ C}_{\text{rel}} = \{\mathbf{I} - [\boldsymbol{\epsilon}\times]\}\mathbf{T}^{C_N}_B\{\mathbf{I} - [\delta\boldsymbol{\theta}\times]\}\mathbf{T}^{B_N}_I\left(\mathbf{R}^I_{\text{moon}} - \mathbf{R}^I_{\text{sc}}\right) \tag{10}$$

The filter propagation equations for the state estimate and error covariance are

$$\dot{\hat{\mathbf{x}}}(t) = \mathbf{f}(\hat{\mathbf{x}}, t) \tag{11}$$

and

$$\dot{\mathbf{P}}(t) = \mathbf{F}(\hat{\mathbf{x}}, t)\mathbf{P}(t) + \mathbf{P}(t)\mathbf{F}^T(\hat{\mathbf{x}}, t) + \mathbf{Q}(t) \tag{12}$$

where $\hat{\mathbf{x}}$ is the filter estimated state vector. The state process noise is given by

$$\mathbf{Q}(t) = \begin{bmatrix} \mathbf{0}_{3\times3} & \mathbf{0}_{3\times3} & \mathbf{0}_{3\times3} & \mathbf{0}_{3\times3} \\ \mathbf{0}_{3\times3} & Q_a\mathbf{I}_{3\times3} & \mathbf{0}_{3\times3} & \mathbf{0}_{3\times3} \\ \mathbf{0}_{3\times3} & \mathbf{0}_{3\times3} & \mathbf{0}_{3\times3} & \mathbf{0}_{3\times3} \\ \mathbf{0}_{3\times3} & \mathbf{0}_{3\times3} & \mathbf{0}_{3\times3} & Q_{\delta\theta}\mathbf{I}_{3\times3} \end{bmatrix} \tag{13}$$

When optical measurements are available, the filter state update and covariance update equations are used.

$$\hat{\mathbf{x}}^{\ +}_k = \hat{\mathbf{x}}^-_k + \mathbf{K}_k[\tilde{z}_k - \hat{z}_k(\hat{\mathbf{x}}^-_k)] \tag{14}$$

$$\mathbf{P}^{\ +}_k = [\mathbf{I} - \mathbf{K}_k\mathbf{H}(\hat{\mathbf{x}}^-_k)]\mathbf{P}^-_k[\mathbf{I} - \mathbf{K}_k\mathbf{H}(\hat{\mathbf{x}}^-_k)]^T + \mathbf{K}_k\mathbf{R}_k\mathbf{K}^T_k \tag{15}$$

where the Kalman gain is

$$\mathbf{K}_k = \mathbf{P}^-_k\mathbf{H}^T_k(\hat{\mathbf{x}}^-_k)[\mathbf{H}_k(\hat{\mathbf{x}}^-_k)\mathbf{P}^-_k\mathbf{H}^T_k(\hat{\mathbf{x}}^-_k) + \mathbf{R}_k]^{-1} \tag{16}$$

The linearized dynamics, $\mathbf{F}$, and the measurement sensitivity matrix [17], $\mathbf{H}$, are given by

$$\mathbf{F}(\hat{\mathbf{x}}, t) = \left.\frac{\partial \mathbf{f}[\mathbf{x}(t), t]}{\partial \mathbf{x}(t)}\right|_{\mathbf{x}(t)=\hat{\mathbf{x}}(t)} \tag{17}$$

$$\mathbf{H}_k(\hat{\mathbf{x}}_k^-) = \left.\frac{\partial \mathbf{h}_k[\mathbf{x}(t_k)]}{\partial \mathbf{x}(t_k)}\right|_{\mathbf{x}(t_k)=\hat{\mathbf{x}}_k^-} \tag{18}$$

where

$$\mathbf{F}(\hat{\mathbf{x}}, t) = \begin{bmatrix} \mathbf{0}_{3\times3} & \mathbf{I}_{3\times3} & \mathbf{0}_{3\times3} & \mathbf{0}_{3\times3} \\ \partial \mathbf{a}_{\text{grav}}^I / \partial \hat{\mathbf{R}}_{\text{sc}}^I & \mathbf{0}_{3\times3} & \mathbf{0}_{3\times3} & \mathbf{0}_{3\times3} \\ \mathbf{0}_{3\times3} & \mathbf{0}_{3\times3} & \mathbf{0}_{3\times3} & \mathbf{0}_{3\times3} \\ \mathbf{0}_{3\times3} & \mathbf{0}_{3\times3} & \mathbf{0}_{3\times3} & \mathbf{I}_{3\times3}/\tau_{\delta\theta} \end{bmatrix} \tag{19}$$

and

$$\mathbf{H} = \begin{bmatrix} 1/R_z & 0 & -R_x/(R_z)^2 \\ 0 & 1/R_z & -R_y/(R_z)^2 \end{bmatrix} \left[-\mathbf{T}_I^C \;\; \mathbf{0}_{3\times3} \;\; \left[\mathbf{R}_{\text{rel}}^{C_N}\times\right] \;\; \mathbf{T}_B^C \left[\mathbf{R}_{\text{rel}}^{B_N}\times\right] \right] \tag{20}$$

It is important to note that for the extended Kalman filter the nonlinear dynamics and measurements are linearized about the filter estimate $\hat{\mathbf{x}}$.

Obtaining statistically significant preflight performance evaluations, as this analysis intends, from an extended Kalman filter typically requires a Monte Carlo analysis. The analysis, requiring perhaps hundreds of simulation runs, would indicate the final covariance of navigation errors and trajectory dispersions or dispersion of the spacecraft from the nominal trajectory at a given time. The downside to Monte Carlo simulations is that they are time and computationally intensive.

D. Linear Covariance

An alternative method for obtaining preflight performance evaluations is a LinCov analysis, generalized by Geller [18] and modified by Stastny. LinCov, based on the continuous–discrete linearized Kalman filter, linearizes the nonlinear dynamics, Eq. (17), and measurements, Eq. (18), about the nominal reference trajectory $\bar{\mathbf{x}}$ rather than the estimated trajectory $\hat{\mathbf{x}}$. This method eliminates the need to estimate the system state while estimating only the error covariance about the nominal trajectory. Ultimately, for most space applications the results are equivalent to those obtained from a similar Monte Carlo analysis [19]. Linearized about the nominal trajectory, the error covariance propagation and update equations become

$$\dot{\mathbf{P}}(t) = \mathbf{F}(\bar{\mathbf{x}}, t)\mathbf{P}(t) + \mathbf{P}(t)\mathbf{F}^T(\bar{\mathbf{x}}, t) + \mathbf{Q}(t) \tag{21}$$

and

$$\mathbf{P}_k^+ = [\mathbf{I} - \mathbf{K}_k\mathbf{H}(\bar{\mathbf{x}}_k^-)]\mathbf{P}_k^-[\mathbf{I} - \mathbf{K}_k\mathbf{H}(\bar{\mathbf{x}}_k^-)]^T + \mathbf{K}_k\mathbf{R}_k\mathbf{K}_k^T$$

The Kalman gain is

$$\mathbf{K}_k = \mathbf{P}_k^-\mathbf{H}_k^T(\bar{\mathbf{x}}_k^-)[\mathbf{H}_k(\bar{\mathbf{x}}_k^-)\mathbf{P}_k^-\mathbf{H}_k^T(\bar{\mathbf{x}}_k^-) + \mathbf{R}_k]^{-1} \tag{22}$$

The new $\mathbf{F}$ and $\mathbf{H}$ matrices, evaluated at the nominal, are defined as

$$\mathbf{F}(\bar{\mathbf{x}}, t) = \left.\frac{\partial \mathbf{f}[\mathbf{x}(t), t]}{\partial \mathbf{x}(t)}\right|_{\mathbf{x}(t)=\bar{\mathbf{x}}(t)} \tag{23}$$

$$\mathbf{H}_k(\bar{\mathbf{x}}_k^-) = \left.\frac{\partial \mathbf{h}_k[\mathbf{x}(t_k)]}{\partial \mathbf{x}(t_k)}\right|_{\mathbf{x}(t_k)=\bar{\mathbf{x}}_k^-} \tag{24}$$

For the analysis, it was assumed that the nominal camera and body frames were aligned. The nominal relative position vector and the measurement sensitivity matrix for the camera focal plane measurement are

$$\mathbf{R}_{\text{rel}}^{C_N} = \mathbf{T}_I^{C_N}\left(\mathbf{R}_{\text{moon}}^I - \mathbf{R}_{\text{sc}}^I\right) \tag{25}$$

$$\mathbf{H} = \begin{bmatrix} 1/R_z & 0 & 0 \\ 0 & 1/R_z & 0 \end{bmatrix} \left[-\mathbf{T}_I^{C_N} \;\; \mathbf{0}_{3\times3} \;\; \left[\mathbf{R}_{\text{rel}}^{C_N}\times\right] \;\; \left[\mathbf{R}_{\text{rel}}^{C_N}\times\right] \right] \tag{26}$$

III. Error Sources

Given the truth model and conceptual Kalman filter, or LinCov filter, there are a series of parameters that affect how the proposed AutoNav system will operate and the OD performance level [20]. These parameters, referred to as the problem parameters, are the primary means of adjusting the analysis algorithms and for determining the AutoNav system's performance and sensitivity to them. The evaluated problem parameters are: 1) the a priori position and velocity knowledge error, 2) the unmodeled accelerations, 3) the spacecraft's attitude knowledge error, 4) the static camera misalignment, 5) the imaging frequency, 6) the Jovian moon ephemeris errors, 7) the camera center-finding bias, 8) the measurement noise, and 9) the number of Jovian moons being imaged. Each problem parameter consists of either a nominal and alternative set point, or a set of quantities. The nominal and alternative settings for the analysis are given in Table 1.

This paper is primarily a sensitivity study to determine which of the aforementioned problem parameters affect the spacecraft's ability to navigate given the autonomous optical approach. The analysis should indicate, among other things, if sensor misalignments need to be calibrated out, if center-finding biases need to be reduced, and to determine if measurement noise levels need to be reduced to achieve a certain level of navigation accuracy.

A. A Priori Covariance

The a priori covariance is the estimation error in the spacecraft's position and velocity relative to Jupiter when it reaches Jupiter's SOI. In practice, the a priori covariance may be fixed by the DSN on earth or determined onboard with additional navigation techniques.

Table 1 Nominal and alternative settings for problem parameters

Problem parameter	Nominal setting ($1-\sigma$)	Alternative setting
A priori knowledge error	100 km and 10 m/s per axis	1000 km and 100 m/s per axis
Unmodeled accelerations	3×10^{-15} m^2/s^3	3×10^{-13} m^2/s^3
Attitude knowledge errors	1 arcsec per axis	10 arcsec per axis
Camera misalignment	0.01 deg per axis	0.1 deg per axis
Imaging frequency	2 h	6 h
Estimated moon ephemerides	75 km	250 km
Image center-finding bias	1% of moon's diameter	5% of moon's diameter
Measurement noise	0.1 pixels in both pixel and line	0.5 pixels in both pixel and line
Moons imaged	12 (see Sec. IV)	17, 27

B. Unmodeled Accelerations

Unmodeled gravitational and nongravitational accelerations are implemented into the analysis as process noise in the LinCov tool and represent the difference between a high-fidelity onboard gravity model and the true gravity. Process noise is modeled as white noise. A worst case acceleration noise level was chosen such that the radial navigation error at perijove would be less than $0.06R_J$ (3-σ) when no measurements are processed. The resulting worst case variance was 3×10^{-13} m^2/s^3. The nominal setting was chosen to correspond to an order of magnitude decrease in the parameter's standard deviation, 3×10^{-15} m^2/s^3.

The "strength" of the white noise accelerations, Q_a, is given in units of m^2/s^3, meaning that the unmodeled accelerations produce a velocity variance (m^2/s^2) that grows at a rate of $Q_a = (m^2/s^2)/s$.

C. Attitude Knowledge Errors

The spacecraft's attitude knowledge errors, modeled by a first-order Markov process, are directly estimated as elements of the filter and are driven by white noise. A standard deviation of 1 arcsec per axis was selected to correspond to the accuracy of a star camera attitude update. The alternative setting is 10 arcsec per axis.

D. Camera Mounting Misalignment

The camera mounting misalignment is directly estimated as an element of the filter. The misalignment error is assumed to be constant with an a priori uncertainty of 0.01 deg per axis. The alternative setting is 0.1 deg per axis. Though this parameter is included in the estimation filter, it is likely that any sensor misalignments would be calibrated out of any real mission.

E. Imaging Frequency

The imaging frequency is limited by the number of optical navigation cameras, likely to be a single camera; the spacecraft's ability to reorient its attitude to point at a new moon; and additional demands on the spacecraft. To minimize reorientation maneuvers, the nominal imaging frequency is to image a new moon every 2 h. The alternative setting is 6 h.

F. Moon Ephemeris Knowledge Errors

Ephemerides for the Jovian moons are obtained from the available SPICE data. Because of the wide range of moons and their varying position accuracies, an average accuracy of the data models was estimated at 75 km (1-σ). Because the direction of the true error is unknown, it is assumed that the estimation error is perpendicular to the spacecraft's line of sight to the moon. The resulting standard deviation of the error in the image measurement is

$$\sigma_{\text{ephem}} = \frac{\Delta r}{r_{\text{sm}}} \tag{27}$$

where Δr is the moon's ephemeris knowledge error and r_{sm} is the range from the spacecraft to the moon. The alternative setting is 250 km.

G. Center-Finding Bias

Captured images must be processed to determine the moon's center-of-mass (CM) pixel location, as opposed to the target's center of brightness (CB). Errors in the CM pixel location resulting from the image processing errors can be modeled as a percentage of the moon's diameter. The standard deviation of the error is

$$\sigma_{\text{CF}} = \frac{\%D}{r_{\text{sm}}} \tag{28}$$

where $\%D$ is the percentage of the moon's diameter. The nominal 1-σ center-finding bias is 1% of the moon's diameter. The alternative setting is 5%. When the imaged moon is relatively close to the spacecraft, this error will dominate. When the imaged moon is further away, this image center-finding bias becomes insignificant and is dominated by measurement noise.

H. Measurement Noise

In addition to center-finding errors, the image processor will experience some level of noise affecting the measurement. Noise affecting the measurements is modeled as white noise with a standard deviation of 0.1 pixels, in both line and pixel measurements of the camera. The alternative setting is 0.5 pixels. A notional camera with a 1 deg field of view was used. The measurement noise assumes a reasonably high signal-to-noise ratio and apparent magnitudes that are well within the capabilities of the camera.

I. Image Processing Model

Because no actual camera or image processing is being performed with the analysis, it is necessary to generate a simple model representing the uncertainty in the AutoNav's measurement of a moon. The variance of the image processing error is modeled as the root of the sum of the squares of the three proceeding error variances.

$$\sigma^2_{\text{measurement}} = \sqrt{(\sigma^2_{\text{inst}})^2 + (\sigma^2_{\text{ephem}})^2 + (\sigma^2_{\text{CF}})^2} \tag{29}$$

The measurement variance is the same in both the line and pixel directions and represents the measurement noise vector $\boldsymbol{\nu}$ in Eq. (8).

IV. Moon Visibility

Three criteria were applied to determine when a moon would be visible to the spacecraft. To be visible, the moon must 1) not be obscured by Jupiter, 2) be outside of a limiting sun cone angle, and 3) be of sufficient visual magnitude to be detected by the navigation camera. A moon's visual magnitude was determined from the moon's absolute magnitude, H, and phase angle relative to the sun. The moon phase angle is calculated as

$$\chi = \cos^{-1}\left[\frac{(\mathbf{R}_J + \mathbf{R}_m) \cdot (\mathbf{R}_m - \mathbf{R}_{\text{sc}})}{|\mathbf{R}_J + \mathbf{R}_m||\mathbf{R}_m - \mathbf{R}_{\text{sc}}|}\right] \tag{30}$$

The moon's apparent visual magnitude is

$$m = H + 2.5\log_{10}\left(\frac{d^2_{\text{MS}} d^2_{\text{MSC}}}{p(\chi) d_0^4}\right) \tag{31}$$

where $p(\chi)$ is the phase integral of a diffuse sphere and is approximated as

$$p(\chi) = \frac{2}{3}\left[\left(1 - \frac{\chi}{\pi}\right)\cos\chi + \left(\frac{1}{\pi}\right)\sin\chi\right] \tag{32}$$

Visibility was evaluated for a limiting sun half cone angle of 45° and for apparent visual magnitudes up to 9.5, [8] 12, and 14. The higher the apparent visual magnitude, the dimmer an object will appear. Moon visibilities, relative to the approach time and nominal spacecraft position, are shown in Fig. 1.

It is important to note that, given a limiting apparent visual magnitude of 9.5 and the additional visibility constraints, only 16 of the included 38 moons are visible to the spacecraft during the approach. Four of these 16 moons, Amalthea (JIV), Thebe (JXIV), Adrastea (JXV), and Metis (JXVI) are within the orbit of Io (JI), and have orbital periods between 7 and 16 h, making their visibility limited and of negligible benefit. These four moons were not considered for possible imaging, leaving 12 possible imaging targets. Increasing the limiting apparent visual magnitude to 12 and 14 increases the number of moons available for imaging to 17 and 27, respectively. The moon visibilities shown are valid for this trajectory only as they are highly dependent on the trajectory geometry relative to Jupiter and its moons and to the sun.

Given the moons available for imaging, a simple imaging sequence was developed for the AutoNav system. The system cycles through the available moons (by Roman numeral designation) selecting a new moon at each imaging sequence. If the next moon is

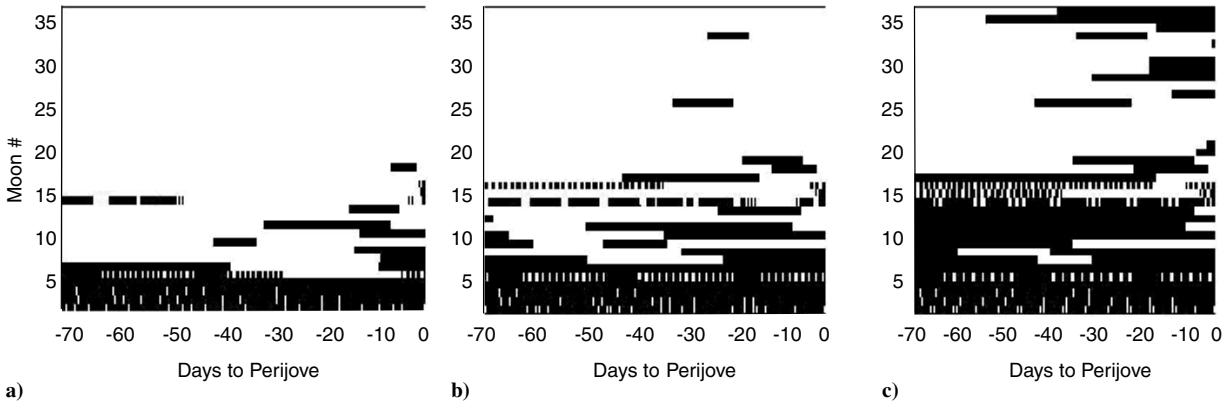

Fig. 1 Jovian moon visibility maps for a limiting apparent visual magnitude: a) 9.5, b) 12, and c) 14. Black regions indicate that the moon is visible to the spacecraft at the given time and nominal position.

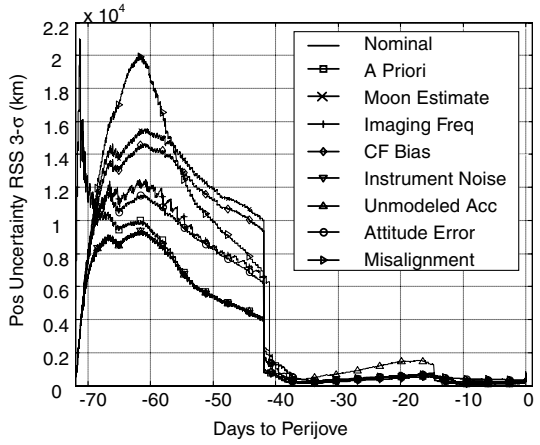

Fig. 2 The 3-σ position uncertainty of the spacecraft from Jupiter's sphere of influence to perijove for each problem parameter setting.

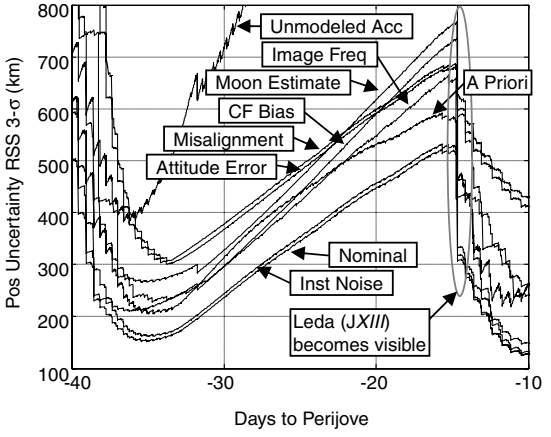

Fig. 4 The 3-σ position uncertainty of the spacecraft from −40 to −10 days to perijove.

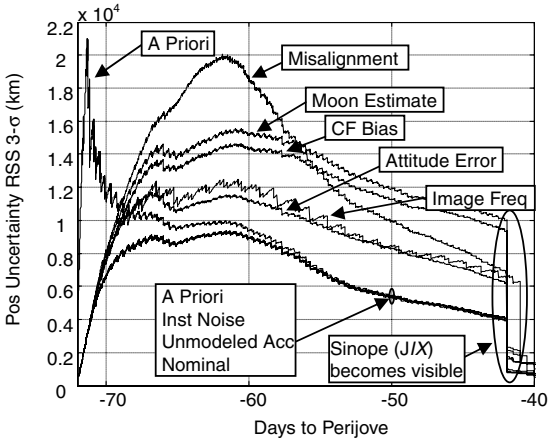

Fig. 3 The 3-σ position uncertainty of the spacecraft from −72 to −40 days to perijove.

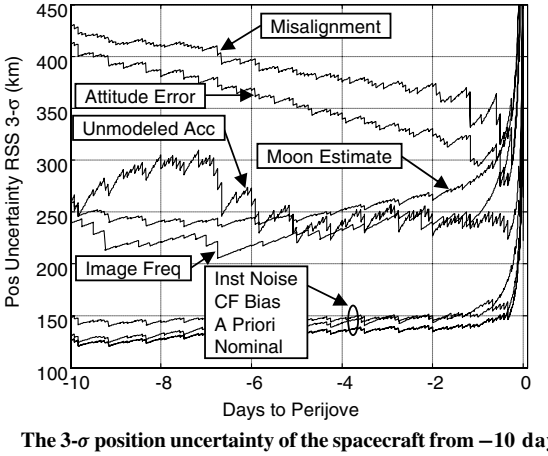

Fig. 5 The 3-σ position uncertainty of the spacecraft from −10 days to perijove through perijove.

not visible at the subsequent imaging sequence, it is skipped and the next available moon is imaged in its place. Though not optimal, this ensures that an image is available at each imaging sequence regardless of the imaging frequency.

V. Results

The LinCov algorithm was implemented to evaluate the performance of the AutoNav system and determine the sensitivity of the navigation errors to the problem parameters. Results were obtained by performing a total of 11 runs corresponding to the nominal and alternative settings of the problem parameters. In the first run, all of the problem parameters were set to their nominal values indicating a likely or best case scenario for the AutoNav system. This run is identified in the results as the *nominal* result. Runs were then performed by switching each problem parameter, one at a time, to its alternative setting. Each of these runs is identified by the problem parameter that was set to its alternative setting for that run.

This approach allows the effects of each problem parameter on the AutoNav navigation error to be evaluated separately. The results were run from Jupiter's SOI (−72 days) to perijove (0 days) with a time step of 5 min. Because of significant differences in the results for the number of moons imaged compared to other parameters, the results for the number of moons imaged are evaluated separately.

It should be noted that these results do not generally indicate improvements over ground-based OD. The results do, however, indicate real-time OD, which has strong implications for time sensitive maneuvers and autonomy. These factors should be considered when comparing the results to ground-based OD.

The results in Fig. 2 show that, for the given parameter settings, the AutoNav system's performance is considerably degraded over the first 40 days of the approach when compared to the a priori knowledge error. This is the first of three distinct phases in the results. During this first phase, shown in Fig. 3, only five moons, the Galilean moons and Himalia (JVI), are visible to the spacecraft's camera. The navigation error is most sensitive to camera misalignment, the moon's estimated position error, and the camera's center-finding bias. The parameters to which the AutoNav system shows minimal sensitivity are the instrument noise, unmodeled accelerations, and the a priori covariance error, which quickly settles to near nominal values. For this phase of the approach, the gravitational model would not be expected to introduce large errors due to the spacecraft's large distance from the planet and steady dynamics. The end of this initial phase is marked by the added visibility of the moon Sinope (JIX) at approximately −42 days to perijove, when the position uncertainty drops sharply for each case.

The second distinct phase, shown in Fig. 4, occurs between −40 and −15 days to perijove. The inclusion of Sinope among the visible moons provides a brief period of increased accuracy followed by a degradation in the position knowledge. Although the effect of most of the parameters increases the navigation error at a fairly consistent rate, the effects of unmodeled accelerations shows increased sensitivities in the system during this phase. This phase ends when the moon Leda (JXIII) becomes visible at approximately −15 days to perijove, again providing a distinct drop in the position uncertainty.

The final phase of the approach is marked by the spacecraft's closest proximity to Jupiter and the Galilean moons, its rapidly changing position and velocity, and the availability of an increased number of moons for imaging. This phase incidentally shows the highest accuracy results for the AutoNav system. During this phase, the AutoNav appears to be most sensitive to the camera mounting misalignment and the spacecraft's attitude knowledge error, both indicating camera pointing errors. Results also indicate an increased sensitivity to the error in the imaged moon's estimated position. Given the spacecraft's proximity to the Galilean moons, increased errors in estimating these moons' positions will result in an increased optical deviation presenting itself similar to a pointing error. The AutoNav system shows the lowest sensitivities to the instrument noise and center-finding biases during this phase. The a priori covariance error has also become negligible as the spacecraft moves to its closest approach. The velocity results are shown in Fig. 6.

Of notable significance in all of these results is the large spike in the position knowledge error and velocity knowledge error (see Figs. 5 and 6) during the final 6–12 h before perijove. This spike is a

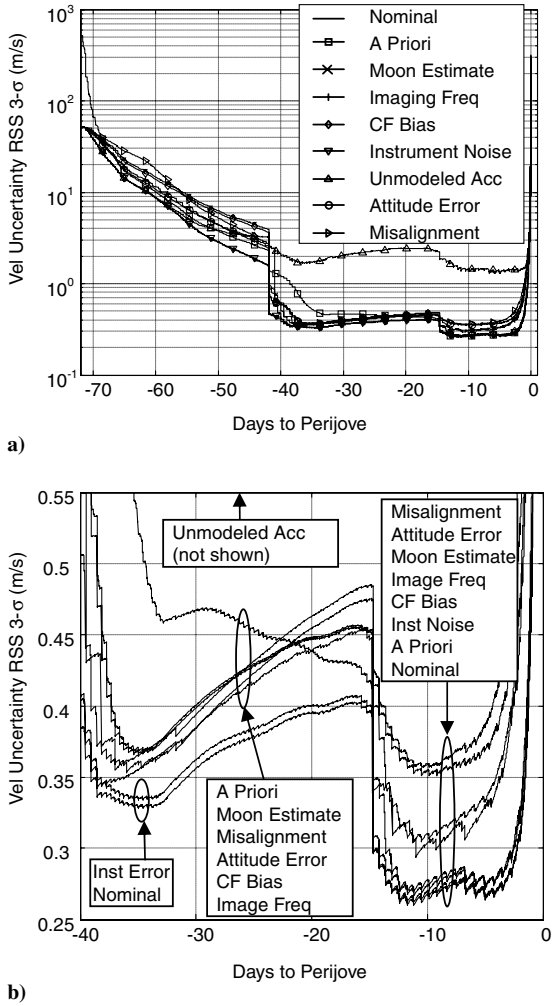

Fig. 6 The 3-σ velocity uncertainty of the spacecraft for each problem parameter setting: a) Jupiter's sphere of influence to perijove, and b) from −40 days to perijove through perijove,

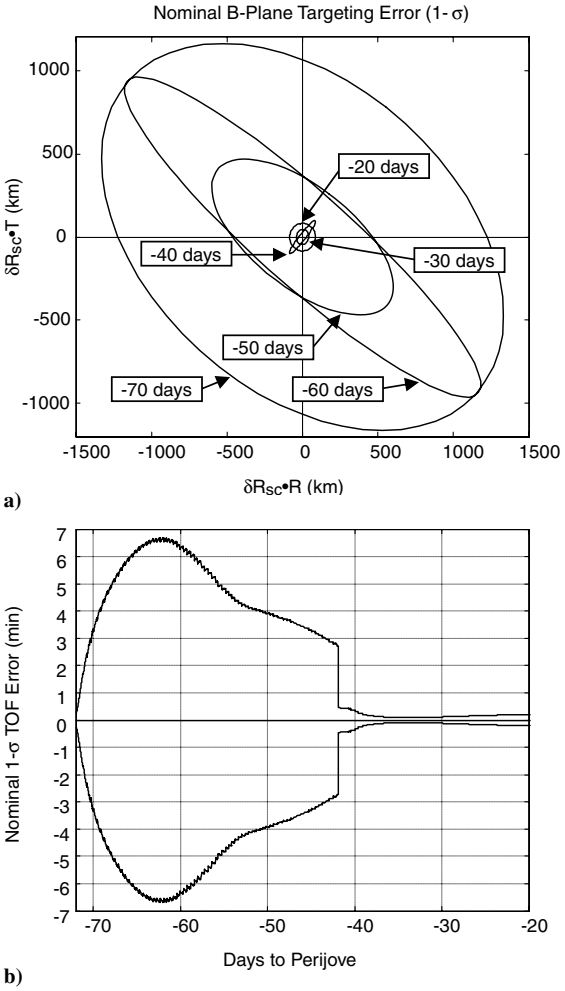

Fig. 7 Targeting errors for the nominal problem parameter settings: a) B-plane targeting errors, and b) time of flight errors.

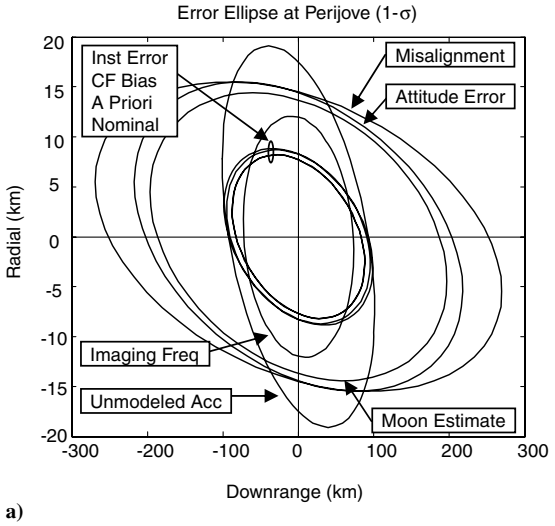

a)

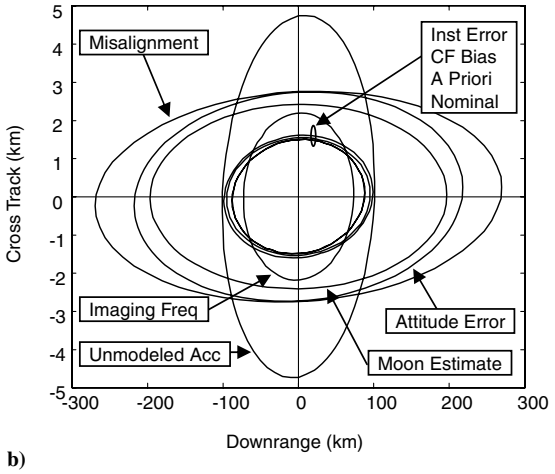

b)

Fig. 8 Local position uncertainty for the spacecraft at perijove for each problem parameter setting: a) radial versus downrange error, and b) cross-track versus downrange error.

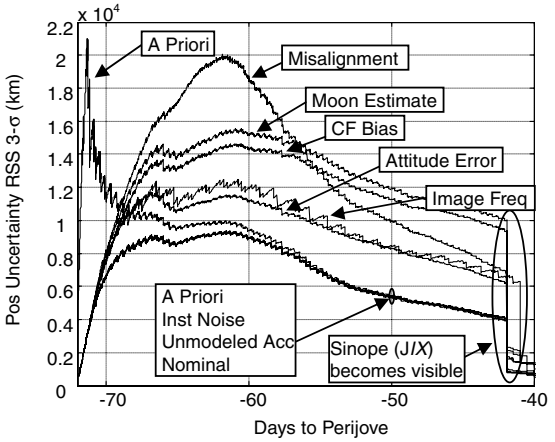

Fig. 9 The 3-σ position uncertainty of the spacecraft from Jupiter's sphere of influence to perijove for varying apparent visual magnitudes detectable to the camera.

result of the spacecraft's nominal orbit and rapidly changing dynamics near perijove and is not due to numerical error.

For hyperbolic approach trajectories, it is of particular importance to understand the amount by which the spacecraft "misses" the planet. This parameter, **B**, is defined as a vector directed from the center of the central body (i.e., Jupiter) to the incoming asymptote of the hyperbola and perpendicular to the asymptote. A unit vector, **S**, is

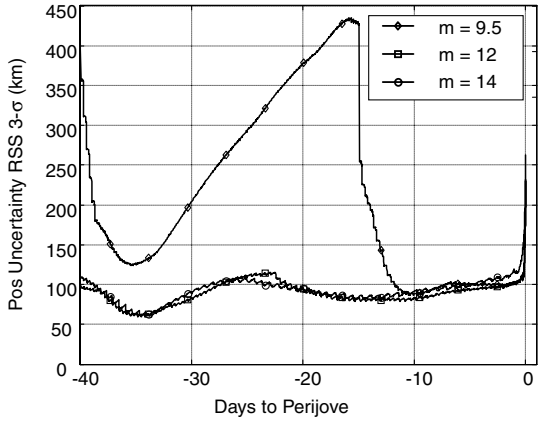

Fig. 10 The 3-σ position uncertainty of the spacecraft from 40 days before perijove through perijove for varying apparent visual magnitudes detectable to the camera.

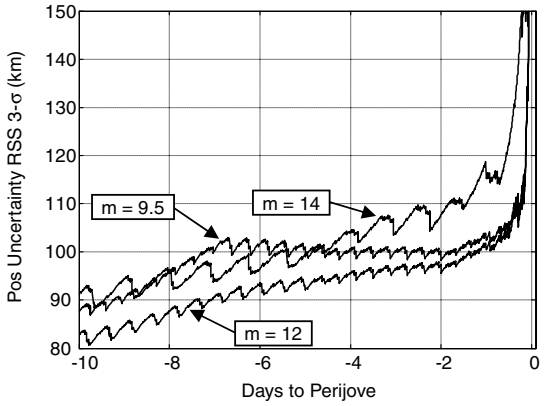

Fig. 11 The 3-σ position uncertainty of the spacecraft from 10 days before perijove through perijove for varying apparent visual magnitudes detectable to the camera.

then defined from the center of the planet and parallel to the incoming asymptote. The vector **B** is resolved into two components, $\mathbf{B} \cdot \mathbf{T}$ and $\mathbf{B} \cdot \mathbf{R}$, where **T** is perpendicular to **S** and lies in a reference plane such as the ecliptic plane. **R** completes the orthogonal coordinate frame. The plane defined by the vectors **T** and **R** is called the "B plane" or the aiming plane and is commonly used for interplanetary navigation. During approach, the spacecraft's inertial position error covariance is mapped to the B plane where it appears as an ellipse. The 1-σ B-plane targeting errors for the nominal parameter settings are shown in Fig. 7a from -70 to -20 days, at ten-day intervals. The corresponding 1-σ time of flight errors are shown in Fig. 7b.

Inspection of the B-plane results shows the AutoNav's sensitivity to the moons being imaged. The significant factor in this sensitivity is the relative geometry of the imaged moons. After an initial growth, the navigation errors show some gradual improvement (-60– -42 days) until Sinope becomes visible and changes the size and correlation of the targeting error. Before this event, four of the five visible moons, the Galilean moons, were nearly aligned geometrically relative to the spacecraft. The addition of Sinope provides measurement information perpendicular to the direction of the Galilean moons. The ability to image moons in a variety of favorable locations relative to the spacecraft is one of the strongest contributors to navigational accuracy.

Although the ability to accurately adjust the approach trajectory is important to mission success, orbit insertion is primarily dependent on the navigation errors at closest approach, or perijove for this mission. At perijove, it is most beneficial to examine the error covariance in a local coordinate frame termed the local–vertical, local–horizontal (LVLH) frame, defined by the radial, downrange, and cross-track directions. The local errors at perijove for the nominal and alternative settings are shown in Fig. 8. The significant

Table 2 3-σ uncertainty in post-maneuver orbital elements

Problem Parameter	i	e	P	R_a
Nominal	90° ±0.0104°	0.9471 ±5.92×10^{-5}	11 days ±22.57 min	$39R_J$[a] ±$0.0382R_J$[a]
A priori covariance	±0.0104°	±5.92×10^{-5}	±22.57 min	±$0.0382R_J$[a]
Ephemeris knowledge error	±0.0179°	±1.29×10^{-4}	±50.60 min	±$0.0856R_J$[a]
Imaging frequency	±0.0161°	±5.09×10^{-5}	±19.01 min	±$0.0321R_J$[a]
Image center-finding biases	±0.0107°	±6.39×10^{-5}	±24.55 min	±$0.0415R_J$[a]
Measurement noise	±0.0113°	±6.65×10^{-5}	±25.36 min	±$0.0429R_J$[a]
Unmodeled accelerations	±0.0265°	±8.09×10^{-5}	±26.82 min	±$0.0454R_J$[a]
Attitude knowledge errors	±0.0211°	±1.43×10^{-4}	±55.87 min	±$0.0945R_J$[a]
Camera misalignment	±0.0212°	±1.74×10^{-5}	±69.35 min	±$0.1173R_J$[a]
Moons imaged ($m = 12$)	±0.0078°	±4.24×10^{-5}	±15.93 min	±$0.0270R_J$[a]
Moons imaged ($m = 14$)	±0.0078°	±5.08×10^{-5}	±19.49 min	±$0.0329R_J$[a]

[a]$R_J = 71,495$ km

error for all parameter settings is the downrange error. The AutoNav's sensitivity to most of the problem parameters results in a general growth of the error ellipse over the nominal settings. The navigation error shows the greatest sensitivity in the downrange error to the camera misalignment, attitude knowledge error, and the estimated moon ephemeris errors. The navigation error shows the greatest sensitivity in the radial and cross-track directions to unmodeled accelerations. Also affecting the radial and cross-track directions are the camera misalignment, attitude knowledge error, estimated moon ephemeris errors, and to a lesser extent the imaging frequency. Although relevant, the sensitivities in the radial and cross-track directions are an order of magnitude smaller than those in the downrange direction. It is interesting to note that reducing the imaging frequency from every 2 h to every 6 h resulted in a decrease in the downrange error at perijove. This "improvement" is likely the result of the nonoptimal imaging sequence and would be negated by an optimal sequence. The value of each moon for navigation at any instant depends on its position relative to the spacecraft and the spacecraft's uncertainty covariance. It appears that the final measurement for the 6 h sequencing provided greater downrange information than the final measurement for the 2 h sequencing.

Results through the various phases of the approach indicate that camera misalignments and attitude knowledge errors are a dominant source of navigation errors. It is recommended that further studies look at using the same camera simultaneously as a star tracker and moon imager to minimize these errors.

It was already stated that the variety of moons available for imaging in terms of relative geometry to the spacecraft greatly affects the AutoNav's performance. To view this sensitivity, additional LinCov analysis was conducted by varying the number of visible moons (see Sec. IV). Error covariance magnitudes for the nominal and two off nominal settings are shown in Figs. 9–11. Figure 9 shows that increasing the camera's imaging capability drastically improves the AutoNav's performance during the initial approach phase by a full order of magnitude. Figures 10 and 11 also show improved navigation errors during the second and third phases, though not as drastic as during the first phase. From approximately 10 days until perijove. the AutoNav system's sensitivity to the additional imaging targets is minimal. The difference in the navigation results during this phase would likely be negated through an optimal imaging sequence in lieu of taking a full day or more to cycle through all available imaging targets.

At perijove, it is assumed that an impulsive maneuver with zero error can be performed to place the spacecraft into a Jupiter orbit. The desired orbit is a polar orbit with a perijove radius of $1.06R_J$ and an apojove radius of $39R_J$. The orbital period is 11 days. Uncertainty in the spacecraft's position and velocity when the maneuver is performed will result in uncertainty in the spacecraft's new orbit. Similar to obtaining the error covariance matrix in the LVLH frame, it is possible to determine the error covariance for the new orbital elements. The orbital elements of greatest interest are the inclination, i, the eccentricity, e, the orbital period, P, and the radius at apojove, R_a. The 3-σ uncertainty in the selected orbital elements given alternative settings for the problem parameters are listed in Table 2. The nominal values for the inclination, eccentricity, period, and apojove radius are also listed with the nominal analysis results.

VI. Conclusions

This paper presented a top-level study analyzing the efficacy of using an autonomous optical navigation system for the approach and orbit insertion phases of a nominal Jupiter mission. The AutoNav system, using optical images of Jupiter's moons for orbit determination, was evaluated for its sensitivity to a range of possible error sources.

Results indicate that the AutoNav system has the greatest sensitivity to the number of moons imaged, which is a function of the imaging camera's optical sensitivity. Specifically, the AutoNav system's performance improves when there are moons at a variety of positions relative to the spacecraft. The system also showed a large sensitivity to line-of-sight pointing errors resulting primarily from attitude knowledge errors of 10 arcsec per axis and camera mounting misalignments of 0.1 deg per axis. Moderate sensitivities were demonstrated from unmodeled accelerations in the spacecraft's gravitational model ($Q_a = 3 \times 10^{-13}$ m^2/s^3), ephemeris estimation errors of the imaged moons (250 km), and the system imaging frequency (6 h). The system also showed lower sensitivities to noise in the imaging instruments (0.5 pixels), possible center-finding biases in the image processing software (5% of the imaged moon's diameter), and a priori knowledge errors (1000 km and 100 m/s).

B-plane targeting and time of flight errors were shown for the nominal trajectory demonstrating the system's sensitivity in the B plane due to the moons being imaged. The final navigation errors at perijove in the downrange, radial, and cross-track directions were also shown for each of the sensitivity parameters analyzed.

References

[1] Hoag, D. G., "The History of Apollo Onboard Guidance, Navigation, and Control," *Journal of Guidance, Control, and Dynamics*, Vol. 6, No. 1, 1983, pp. 4–13.

[2] Riedel, J. E., Bhaskaran, S., Synnott, S. P., Bollman, W. E., and Null, G. W., "An Autonomous Optical Navigation and Control System for Interplanetary Exploration Missions," International Academy of Astronautics Paper L-506, April 1996.

[3] Campbell, J. K., Jacobson, R. A., Riedel, J. E., Synnott, S. P., and Taylor, A. H., "Voyager 1 and Voyager 2 Saturn Encounter Orbit Determination," AIAA Paper 82-419, Jan. 1982.

[4] Campbell, J. K., Synnot, S. P., and Bierman, G. J., "Voyager Orbit Determination at Jupiter," *IEEE Transactions on Automatic Control*, Vol. 28, No. 3, March 1983, pp. 256–268. doi:10.1109/TAC.1983.1103223

[5] Riedel, J. E., Owen, W. M., Jr., Stuve, J. A., Synnott, S. P., and Vaughan, R. M., "Optical Navigation During the Voyager Neptune Encounter," AIAA Paper 90-2877, Aug. 1990.

[6] Taylor, A. H., Jacobson, R. A., Synnott, S. P., Lewis, G. D., and Riedel, J. E., "Orbit Determination for the Voyager II Uranus Encounter," AIAA Paper 86-2112, Aug. 1986.

[7] Riedel, J. E., Bhaskaran, S., Synnot, S. P., Desai, S. D., Bollman, W. E., Dumont, P. J., Halsell, C. A., Han, D., Kennedy, B. M., Null, G. W.,

Owen, W. M., Jr., Werner, R. A., and Williams, B. G., "Navigation for the New Millennium: Autonomous Navigation for Deep Space 1," *Proceedings of the 12th International Symposium on Space Flight Dynamics*, SP-403, ESA, Paris, June 1997, pp. 303–320.

[8] Bhaskaran, S., Riedel, J. E., Synnott, S. P., and Wang, T. C., "The Deep Space 1 Autonomous Navigation System: A Post-Flight Analysis," AIAA Paper 00-3935, Aug. 2000.

[9] Ondrasik, V. J., Ransford, G. A., and Hildebrand, C. E., "An Analysis of Outer Planet Navigation Systems," AIAA Paper 72-926, Sept. 1972.

[10] Russell, R. K., and Ellis, J., "Orbit Determination for a Jupiter Orbiter Tour of the Galilean Satellites," *Journal of Spacecraft and Rockets*, Vol. 12, No. 6, 1975, pp. 368–373.

[11] Gelb, A., *Applied Optimal Estimation*, MIT Press, Cambridge, MA, 1974, Chaps. 6–7.

[12] Yong, K., Chao, C. C., and Liu, A. S., "Autonomous Navigation for Satellites Using Lasercom Systems," AIAA Paper 83-428, Jan. 1983.

[13] Gounley, R., White, R., and Gai, E., "Autonomous Satellite Navigation by Stellar Refraction," *Journal of Guidance, Control, and Dynamics*, Vol. 7, No. 2, 1984, pp. 129–134.

[14] Tuckness, D. G., "Precision Landing on Mars Using Imaging Penetrator Beacons," *Journal of Spacecraft and Rockets*, Vol. 31, No. 6, 1994, pp. 1085–1091.

[15] Burkhart, P. D., and Bishop, R. H., "Adaptive Orbit Determination for Interplanetary Spacecraft," *Journal of Guidance, Control, and Dynamics*, Vol. 19, No. 3, 1996, pp. 693–701.

[16] Matousek, S., "The Juno New Frontiers Mission," International Astronautical Congress Paper 05-A3.2.A.04, Oct. 2005.

[17] Pittelkau, M. E., "Rotation Vector in Attitude Estimation," *Journal of Guidance, Control, and Dynamics*, Vol. 26, No. 6, 2003, pp. 855–860.

[18] Geller, D. K., "Linear Covariance Techniques for Orbital Rendezvous Analysis and Autonomous Onboard Mission Planning," *Journal of Guidance, Control, and Dynamics*, Vol. 29, No. 6, 2006, pp. 1404–1414.

[19] Woffinden, D. C., and Geller, D. K., "Relative Angles-Only Navigation and Pose Estimation for Autonomous Orbital Rendezvous," AIAA Paper 06-6300, Aug. 2006.

[20] Rush, B., Bhaskaran, S., and Synnott, S. P., "Improving Mars Approach Navigation Using Optical Data," American Astronautical Society Paper 01-412, July 2001.

B. Marchand
Associate Editor